# In situ electrochemical oxidation of $Cu_2S$ into CuO nanowires as a durable and efficient electrocatalyst for oxygen evolution reaction

Yong Zuo[a,b], Yongpeng Liu[c], Junshan Li[a,b], Ruifeng Du[a,b], Xu Han[d], Ting Zhang[d], Jordi Arbiol[d,e], Núria J. Divins[f], Jordi Llorca[f], Néstor Guijarro[c], Kevin Sivula[c], Andreu Cabot[a,e,*]

[a] Catalonia Institute for Energy Research – IREC, Sant Adrià de Besòs, Barcelona 08930, Spain

[b] Departament d'Electronica, Universitat de Barcelona, 08028 Barcelona, Spain

[c] Laboratory for Molecular Engineering of Optoelectronic Nanomaterials (LIMNO), École Polytechnique Fédérale de Lausanne (EPFL), Station 6, CH-1015 Lausanne, Switzerland

[d] Catalan Institute of Nanoscience and Nanotechnology (ICN2), CSIC and BIST, Campus UAB, Bellaterra, 08193 Barcelona, Spain

[e] ICREA, Pg. Lluís Companys 23, 08010 Barcelona, Spain

[f] Institute of Energy Technologies, Department of Chemical Engineering and Barcelona Research Center in Multiscale Science and Engineering, Universitat Politècnica de Catalunya, EEBE, 08019 Barcelona, Spain

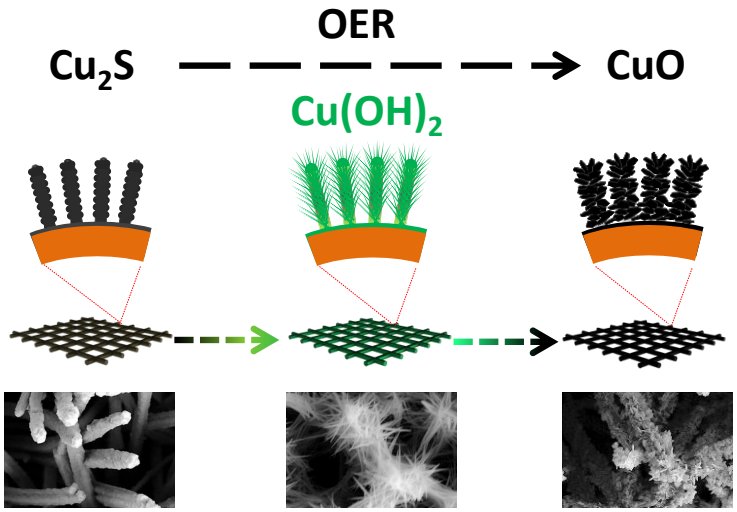

**ABSTRACT:** Development of cost-effective oxygen evolution catalysts is a task of capital importance for the deployment of large scale energy storage systems based on metal-air batteries and reversible fuel cells. In this direction, a wide range of materials have been explored. Among other, several metal chalcogenides have demonstrated excellent performances. However, chalcogenides are thermodynamically less stable than the corresponding oxides and hydroxides under oxidizing potentials and can be chemically transformed during oxygen evolution in alkaline media. While this instability has prevented in some cases their application as oxygen evolution catalysts and it has been disregarded in some other, we propose to use it in our favor to produce a high performance copper-based oxygen evolution catalyst. We characterize here the in situ chemical, structural and morphological transformation during the oxygen evolution reaction (OER) in alkaline media of $Cu_2S$ into CuO nanowires (NWs), mediating the intermediate formation of $Cu(OH)_2$. We also test their OER activity and their stability under OER operation in alkaline media, and compare it with the OER performance of $Cu(OH)_2$ and CuO nanostructures directly grown on the surface of a copper mesh. We demonstrate here that CuO produced during OER from $Cu_2S$ displays extraordinary electrocatalytic performance toward OER, well above that of copper oxide synthesized mediating no OER in situ transformation.

# 1. INTRODUCTION

Driven by energy and environmental crises resulting from the fast consumption of fossil fuels, the share of renewable energies such as wind and photovoltaics is steadily growing. To sustain this growth, besides increasing cost-efficiency of the generation technologies, we need to find solutions for large scale and distributed power storage systems that are able to compensate for the fluctuating character of these energy supplies. In this direction, metal-air batteries, reversible fuel cells and electrolysers are the most promising technologies for large scale energy storage, but all of them are limited by the same essential and sluggish reaction step: oxygen evolution.[1–3]The oxygen evolution reaction (OER) involves breaking O-H bonds to form O=O bonds, what comprises four sequential proton-coupled electron transfer steps.[4–7] Currently noble metals are used to catalyze this reaction, but activities and stabilities are still not satisfactory and the high cost of these catalysts compromises the system cost-effective. Thus the development of highly efficient and robust OER catalysts based on earth-abundant elements is a topic of capital importance.[8–13]

Transition metal oxides and (oxy)hydroxides are the main alternative to noble metals as OER catalysts, reaching performances close to those of $IrO_2$/$RuO_2$ in alkaline media.[14,15] Additionally, several reports have claimed metal phosphides,[16–18] nitrides,[19–22] selenides[23,24] and sulfides[25–28] to be excellent OER catalysts. However, some of these compounds are thermodynamically unstable under harsh OER conditions and may suffer chemical transformation during operation.[2,6,29–31] While this instability has been ignored in most studies, when analyzed in detail, excellent performances obtained for chalcogenides and pnictides have in some cases been related not to the chalcogenide or pnictide cations, but to the in situ formed oxide or (oxy)hydroxide.[32–39] For example, the surface of $CoS_x$[40] and NiS,[27] would oxidize to the corresponding oxide/(oxy)hydroxide species (always presented as amorphous) to generate the core-shell structure with superior activity in OER operation. This oxidation phenomenon in OER case has also been seen in other metal-based electrocatalysts such as NiSe,[6] CoP,[41] CoN,[42] $Ni_xFe_{1-x}Se_2$,[43] $Co_{0.6}Fe_{0.4}P$,[44] etc.

The outstanding performances measured from oxides and hydroxides grown during OER operation may have different origins: i) During the in situ growth of the oxide/hydroxide nanostructured material, avenues for effective electrolyte diffusion may be created; ii) During the

rapid chemical transformation at ambient temperature, an increase of the surface area through the material recrystallization in the form of smaller crystallites may be obtained. iii) A high density of defects, including ion vacancies, grain boundaries and metastable phases, may be obtained in these growth conditions; iv) New catalytic sites with higher activity may be in situ created due to the intimate relation between the structure growth and the electrocatalytic OER process; v) Residual chalcogen and phosphorous cations may remain on the surface providing favorable catalytic sites. [45–48]

Herein, we report on the chemical, structural and morphological transformation during OER operation of $Cu_2S$ nanowires (NWs) grown on the surface of a copper mesh (CM). We further investigate the effect that these transformations have on the OER activity of $Cu_2S$ and $Cu_2S$-derived nanostructures and demonstrate the OER performance of the compound in situ formed during operation to outperform that of the same compound obtained by other processes, both in terms of activity and stability.

## 2. EXPERIMENTAL SECTION

**Chemicals:** Ammonium persulfate (APS, $(NH_4)_2S_2O_8$, ≥98.0 %) and sodium sulfide nonahydrate ($Na_2S{\cdot}9H_2O$, ≥98.0 %) were purchased from Aldrich. Sodium hydroxide (NaOH, 98.5 %) was purchased from Acros. All chemicals were used as received without further purification. Cu mesh (CM) with a wire diameter of about 200 μm and a pore size of 400 μm, and Cu foam (CF) with a thickness of 1 mm and a pore size of 120 PPI were purchased from Kunshan GuangJiaYuan new materials Co. Ltd. Deionized water (DW, 18.6 MΩ/cm) obtained using a purification system (Mini-Q Water) was used for all experiments.

**Synthesis of $Cu(OH)_2$/CM:** $Cu(OH)_2$ NWs on CM ($Cu(OH)_2$/CM) were prepared following an earlier report with some modifications.[49,50] Briefly, a piece of CM (2.5 cm×1 cm) was thoroughly cleaned using ethanol/acetone and HCl (5 mol/L) for 30 minutes, and then rinsed with plenty of DW. The cleaned CM was then immersed in a solution of NaOH (40 mmol), APS (2 mmol) and DW (20 mL) at room temperature for 30 min. The obtained $Cu(OH)_2$/CM was then washed carefully using DW and then dried using nitrogen flow.

**Synthesis of $Cu_2S$/CM:** $Cu_2S$ NWs on CM ($Cu_2S$/CM) were prepared by an anion exchange route. $Cu(OH)_2$/CM were immersed in a $Na_2S$ solution (20 mL DW, 0.1 mol/L) for 1 h at 60 °C. The obtained black $Cu_2S$/CM was carefully washed using DW and ethanol and then dried naturally.

**Synthesis of CuO/CM-AN:** CuO NWs on Cu mesh (CuO/CM-AN) were prepared by annealing $Cu(OH)_2$/CM under Ar atmosphere for 2 h at 200 °C, reached using a temperature ramp of 5 °C/min. The obtained CuO/CM-AN was collected without any further treatment.

**Synthesis of $Cu_2S$/CF:** $Cu_2S$ NWs on CF ($Cu_2S$/CF) were prepared using a similar procedure as the one used to produce $Cu_2S$/CM, but using a CF instead of a CM and increasing the sulfurization time to 2 h to complete the ion exchange.

**Materials characterization:** X-ray diffraction (XRD) patterns were obtained on a Bruker AXS D8 Advance X-ray diffractometer (Bruker, Karlsruhe, Germany) operating at 40 kV and 40 mA with Ni-filtered (2 μm thickness) Cu Kα1 radiation (λ = 1.5406 Å). Scanning electron microscope (SEM) analysis was carried out in a Zeiss Auriga microscope (Carl Zeiss, Jena, Germany) with an energy dispersive X-ray spectroscopy (EDX) detector at 20 kV to study composition. Transmission electron microscopy (TEM) characterization was carried out on a

Zeiss Libra 120 (Carl Zeiss, Jena, Germany), operating at 120 kV. High-resolution TEM (HRTEM) images were obtained using a field emission gun FEI Tecnai F20 microscope at 200 kV with a point-to-point resolution of 0.19 nm. High angle annular dark-field (HAADF) STEM was combined with electron energy loss spectroscopy (EELS) in the Tecnai microscope by using a Gatan Quantum filter. For TEM characterization, tiny powder samples were carefully collected by folding the Cu substrate to peel the surface materials. The collected powder was dispersed in ethanol by 30 s sonication and then drop casted on a 200 mesh copper grid. X-ray photoelectron spectroscopy (XPS) was carried out on a Specs system (Specs GmbH, Berlin, Germany) equipped with a Mg anode XR50 source operating at 250 mW and a Phoibos 150 MCD-9 detector (Specs GmbH, Berlin, Germany). The pressure in the analysis chamber was kept below $10^{-7}$ Pa. Data processing was performed with the CasaXPS program (Casa Software Ltd., UK). Binding energy (BE) values were centered by using the C 1s peak at 284.8 eV.

**Electrochemical measurements:** Electrochemical measurements were conducted in a three-electrode system using an electrochemical workstation (Metrohm Autolab). Characterized samples were used as working electrode (partially cut to leave the working area as 1×1 cm); while a graphite rod with a diameter of 6 mm was used as the counter electrode and a Hg/HgO (1 M KOH, 0.098 V *vs.* RHE) was applied as the reference electrode. 1 M KOH was used as electrolyte. The electrolyte was purged with $O_2$ for 30 min prior to each measurement. The following formula was used to convert the potentials to the reversible hydrogen electrode (RHE) standard scale:

$$E \textit{ vs. } RHE = E_{Hg/HgO} + E^{o}_{Hg/HgO} + 0.059 \times pH = E_{Hg/HgO} + 0.924 \text{ (V)}$$

While the following formula was applied to calculate the overpotentials:

$$\eta = E - 1.23 \text{ (V)} = E_{Hg/HgO} - 0.306 \text{ (V)}$$

Polarization curves were obtained using cyclic voltammetry (CV) at 100 mV/s when analyzing chemical transformations and at 5 mV/s when analyzing OER performance. Structural, chemical and morphological characterization of the electrodes after operation/activation was carried out by cutting a small piece of working electrode (*ca.* 3×3mm triangle). All tests were done under static circumstance without a magnet bar stirring on bottom. All the experiments were performed at room temperature of ca. 15 $^{o}$C.

**Electrochemical surface area (ECSA):** To estimate the effective ECSA, CV measurements were conducted to check the electrochemical double layer capacitance of samples at the non-faradic potential region to. Typically, a series of CV were performed at various scan rates (10 mV/s, 20 mV/s, 40 mV/s, etc.) in 1.22-1.32 V *vs.* RHE. The double layer capacitance ($C_{dl}$) was determined using the equation $\Delta J/2 = \nu \times C_{dl}$, in which $\Delta J$ corresponds to the current density between the anodic and cathodic sweeps at 1.27 V *vs.* RHE against the scan rate. The slope of the fitting line is equal to twice of the $C_{dl}$ value, which is proportional to the electrochemical surface area of the materials. This comparison makes sense only when the measurements of materials are carried out under the same condition.

**Electrochemical impedance spectroscopy (EIS):** EIS was conducted on the working electrodes under the OER operating conditions at the anodic bias that delivered a geometric current density of ~10 mA/cm$^2$ (0.68 V *vs.* Hg/HgO). A sinusoidal voltage with amplitude of 10 mV and a scanning frequency ranging from 100 mHz to 1 MHz was applied to carry out the measurements.

**iR correction:** The OER curves in this work are shown without iR correction. However, to display the accurate performance on OER operation, we did iR correction towards the overpotential that delivers a geometric current density of 10 mA/cm$^2$ according to the following formula:

$$\eta_{corrected} = \eta - iR_s \times 90\ \%$$

$R_s$ indicates the electrolyte solution resistance and can be measured using EIS. In our work, the $R_s$ was measured as 4.7 **Ω** at 10 mA/cm$^2$ for electrode of $Cu_2S$-derived CuO/CM.

**In-situ Raman spectroscopy:** In-situ Raman measurements were performed with a Raman microscope (Horiba Jobin Yvon XploRA PLUS) coupled to an optical microscope (Olympus BX41). The objective lens (Olympus MPlan N, 50×, NA=0.75) was covered with optically transparent Teflon film (American Durafilm 50A, 0.013 mm) to prevent potential damage from electrolytes. Raman excitation was provided by a 532 nm laser (Horiba DPSS). A 3-electrode configuration was set up in a 3D printed Raman electrochemical cell that was fit onto the manual Olympus XY stage. The 3-electrode configuration was connected to a Bio-Logic SP-50 potentiostat.

## 3. RESULTS AND DISCUSSION

$Cu(OH)_2$ NWs were grown at the surface of a CM by immersing it in an aqueous solution of NaOH/APS for 30 min. During this process, the initial reddish brown CM turned greenish-blue (Figure S1a). XRD patterns (Figure 1a) of the produced layers fitted well with the standard JCPDF card #13-0420 corresponding to $Cu(OH)_2$. SEM micrographs of $Cu(OH)_2$/CM displayed a homogeneous distribution of faceted NWs with an average thickness of *ca.* 200 nm (Figures 1b) and an average length of *ca.* 15 μm (Figure Sx). The growth mechanism of $Cu(OH)_2$ NWs from Cu surfaces was previously described and it is illustrated in Figure S1d.[51] Briefly, surface Cu is oxidized by $S_2O_8^{2-}$ ions to $Cu^{2+}$, which immediately reacts with $OH^-$ in solution to subsequently recrystallize $Cu(OH)_2$ nanostructures on the CM surface.[51]

$Cu(OH)_2$/CM was sulfurized by immersion in a $Na_2S$ solution (Figure 1c). During this transformation, the layer color changed from greenish-blue to black (Figure S1a). XRD analysis showed the produced layers to display a hexagonal $Cu_2S$ crystal phase (JCPDS #23-0961), with no evidence of crystalline $Cu_xO$ impurities. EDX analyses confirmed the atomic ratio between Cu and S to be close to that of stoichiometric $Cu_2S$ (Figure S2). $Cu_2S$ nanostructures maintained the original $Cu(OH)_2$ NW geometry, but displayed much rougher surfaces that contained flake-like crystallites with an average size of *ca.* 50 nm in diameter and *ca.* 10 nm in thickness (Figures 1c, 1d, S1c). HRTEM analysis confirmed the crystallographic phase of the crystallites to match that of hexagonal $Cu_2S$ (space group = P63/mmc) with a=b=3.8900 Å and c=6.6800 Å (Figure 1d, right side). EELS chemical composition maps displayed an homogeneous distribution of both Cu and S throughout the NWs (Figure 1e).

XPS analysis of $Cu_2S$/CM (Figure 1f) displayed a main Cu 2p doublet at 932.7 eV (Cu $2p_{3/2}$), corresponding to $Cu^0$ and/or $Cu^+$ species.[52,53] The presence of a small satellite peak at ca. 945 eV revealed the existence of a $Cu^{2+}$ contribution, which accounted for less than 10 % of the total measured copper. This contribution may result from a partial surface oxidation upon exposure to ambient atmosphere.[54] The Cu LMM Auger spectrum was analyzed to differentiate between $Cu^0$ and $Cu^+$ components. As displayed in Figure 1f, the Cu LMM signal could be fitted assuming a main $Cu_2S$ component and a minor CuO contribution[55,56] accounting for *ca.* 10 % of the total Cu, in agreement with the deconvolution of the Cu 2p region.

The S 2p XPS spectrum displayed two well-defined doublets at 162.2 eV (S $2p_{3/2}$) and 169.1 eV (S $2p_{3/2}$) that were assigned to lattice S in $Cu_2S$ and to sulfate species arising from the surface oxidation of the material, respectively.[54,57–62] Sulfates accounted for *ca.* 14 % of the total amount of sulfur detected.

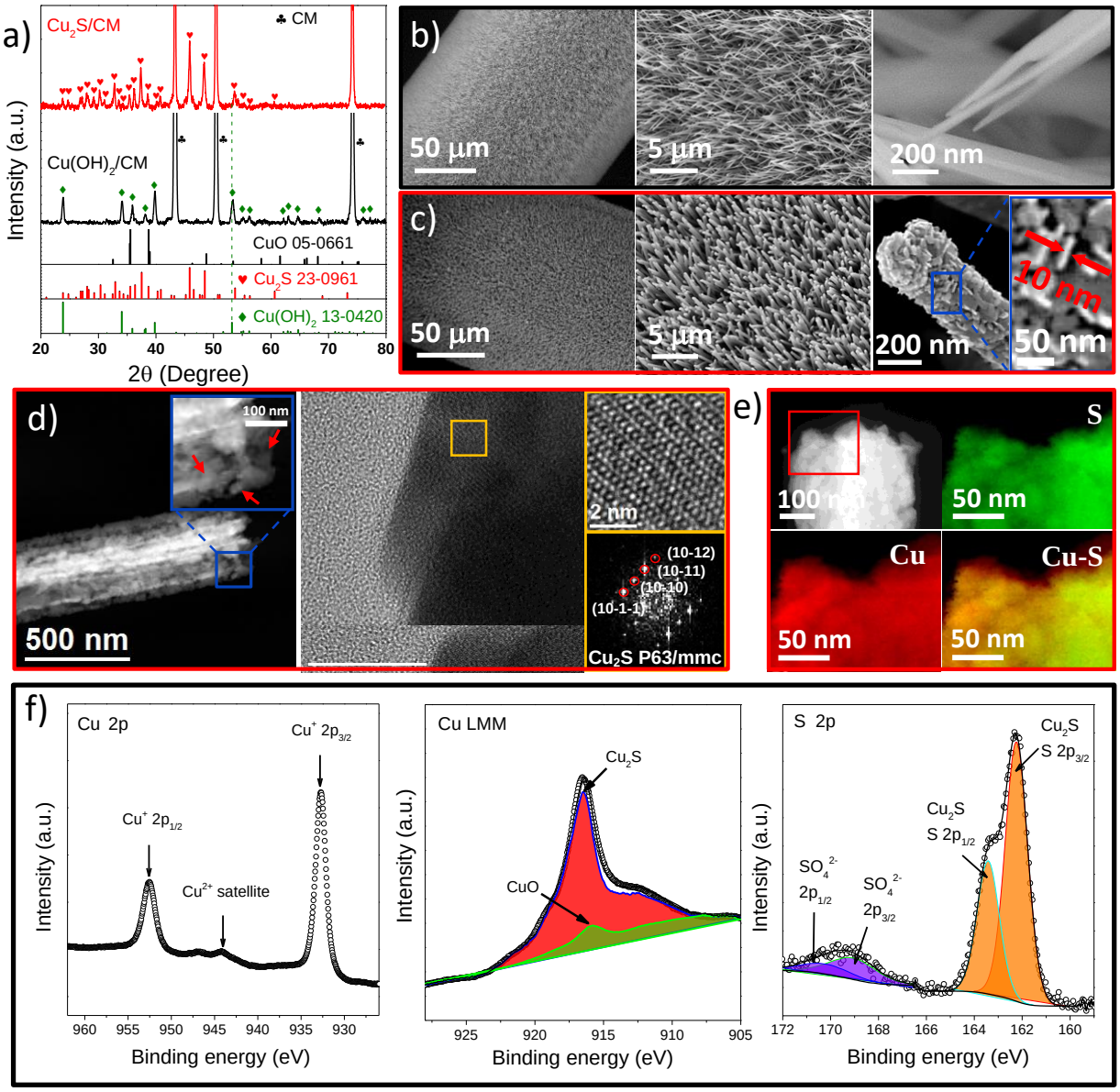


**Figure 1**. (a) XRD patterns of $Cu(OH)_2$/CM and $Cu_2S$/CM. (b,c) SEM images of (b) $Cu(OH)_2$/CM and (c) $Cu_2S$/CM. (d) TEM and HRTEM micrographs of a $Cu_2S$ NW. From the crystalline domain displayed, the $Cu_2S$ lattice fringe distances were measured to be 0.236 nm, 0.296 nm, 0.342 nm and 0.311 nm, at 18.65º, 45.93º and 72.42º, which was interpreted as the hexagonal $Cu_2S$ phase visualized along its [-12-10] zone axis. (e) STEM micrograph and EELS chemical composition maps obtained from the red squared area of

the STEM micrograph: Individual Cu $L_{2,3}$-edges at 931 eV (red) and S $L_{2,3}$-edges at 165 eV (green) as well as its composite. (f) Cu 2p, Cu LMM and S 2p regions of the XPS spectrum of $Cu_2S$/CM.

$Cu_2S$/CM electrodes were cycled in the potential range 0-0.8 V *vs.* Hg/HgO at scan rate of 100 mV/s while immersed in a 1 M KOH electrolyte solution. During the initial 50 CV cycles, a drastic change of electrochemical performance was observed (Figure 2a). The first several CVs provided a relatively linear dependence of the current density with the applied potential. This current density rapidly decreased with the cycle number, pointing at an intense chemical transformation of the working electrode. After 150 cycles, the electrochemical response was stabilized (Figure 2b, S3a-b). Figure 2c displays a series of quasi-stationary CVs measured at a slow scan rate of 5 mV/s on the initial $Cu_2S$/CM and after 50, 100 and 200 CV cycles ($Cu_2S$/CM_50CVs; $Cu_2S$/CM_100CVs; $Cu_2S$/CM_200CVs). High oxidation currents were obtained from the initial $Cu_2S$/CM electrodes and only after ca. 100 CV cycles a conventional and stable OER curve was measured (Figure 2c,d).

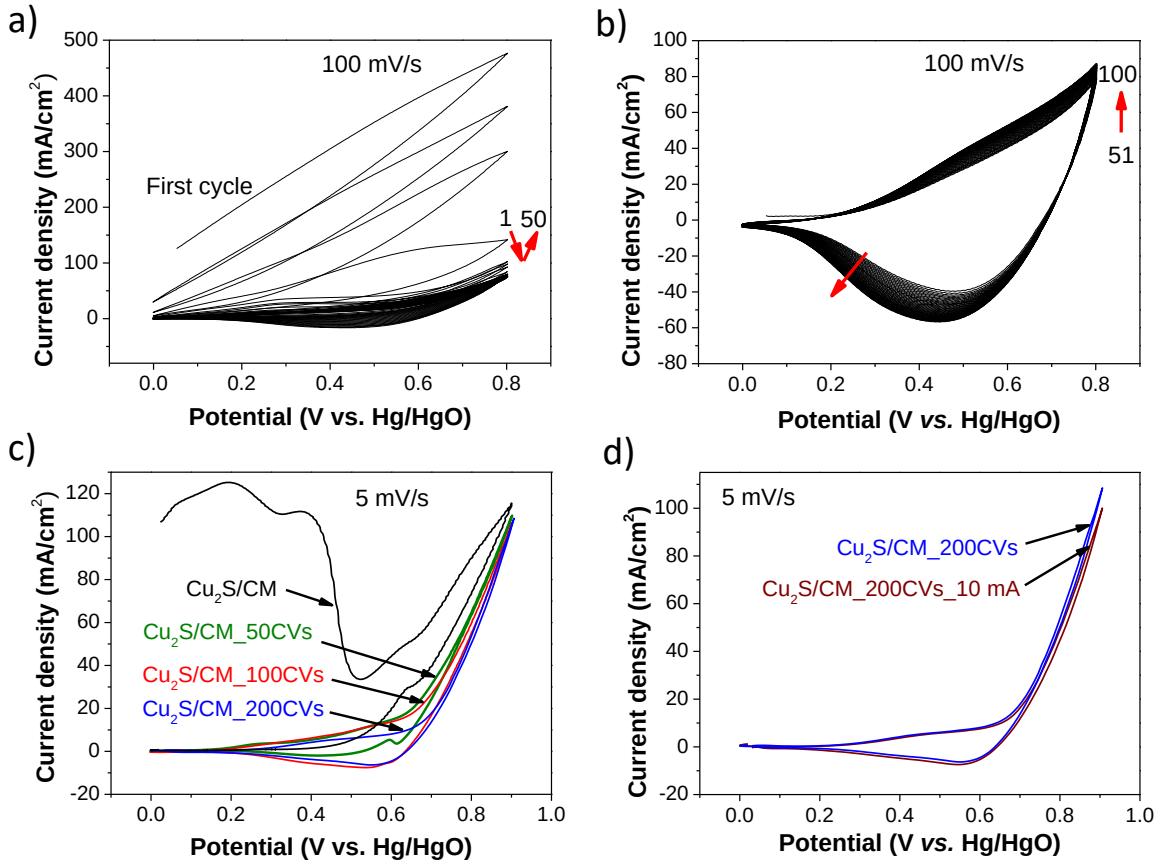


**Figure 2.** (a,b) Multiple CVs of $Cu_2S$/CM: (a) 1-50 cycles; (b) 51-100 cycles; (c) 101-150 cycles. Scan rate: 100 mV/s. (c,d) Quasi-stationary polarization CVs obtained at 5 mV/s of $Cu_2S$/CM: (c) after

different activation CVs at 100 mV/s, and (d) after 200 CVs at 100 mV/s and before/after chronopotentiometry measurement at a geometric current density of 10 mA/cm$^2$ for 10000 s. Scan rate: 5 mV/s.

SEM analysis of $Cu_2S$/CM electrodes showed the initial $Cu_2S$ NWs to develop thin nanofibers that interconnected into networks after 50 CVs (Figure 3a-b). After 100 CVs nanofibers had grouped into bundles, which evolved again into nanoflake-based NWs as cycling continued (Figure 3c-d). Final stable NWs obtained after *ca.* 150 CVs were slightly thicker than the initial ones, *ca.* 400 nm, conserved a similar length, *ca.* 15 μm, and were composed of slightly larger nanoflakes (*ca.* 150 nm in diameter, *ca.* 10 nm in thickness) that grouped less compactly than in the original $Cu_2S$ NWs, thus providing a more porous NW structure.

XRD analysis demonstrated the initial $Cu_2S$ to be transformed into $Cu(OH)_2$ after 50 CVs, and to have evolved to CuO after 200 CVs at 100 mV/s (Figure 3e). To track the composition evolution in more detail, in-situ Raman spectroscopy was performed on freshly prepared $Cu_2S$/CM samples after 10, 20, 50, 100, and 200 CVs at 100 mV/s. As shown in Figure 3f, the initial $Cu_2S$/CM exhibited two characteristic Raman peaks at 266 cm$^{-1}$ (Cu–S bond)[63,64] and 472 cm$^{-1}$ (S–S bond),[63,64] that corresponded to $Cu_2S$. A similar spectrum was obtained after 10 CVs. After 20 CVs, the intensity of the main peak at 472 cm$^{-1}$ dramatically decreased and new peaks appeared. After 50 CVs, Raman spectra evidenced the presence of $Cu(OH)_2$, with two characteristic peaks at 290 cm$^{-1}$ and 488 cm$^{-1}$.[65] An additional weak peak at 633 cm$^{-1}$ could be assigned to the presence of a copper oxide phase.[65] After extensive cycling, the initial $Cu_2S$/CM had completely transformed to CuO, which displayed three characteristic Raman peaks at 290 cm$^{-1}$ (Cu–O bond, $A_g$ phonon mode),[65] 340 cm$^{-1}$ (Cu–O bond, $B_{1g}$ phonon mode),[65,66] and 623 cm$^{-1}$ (Cu–O bond, $B_{2g}$ phonon mode).[65,66]

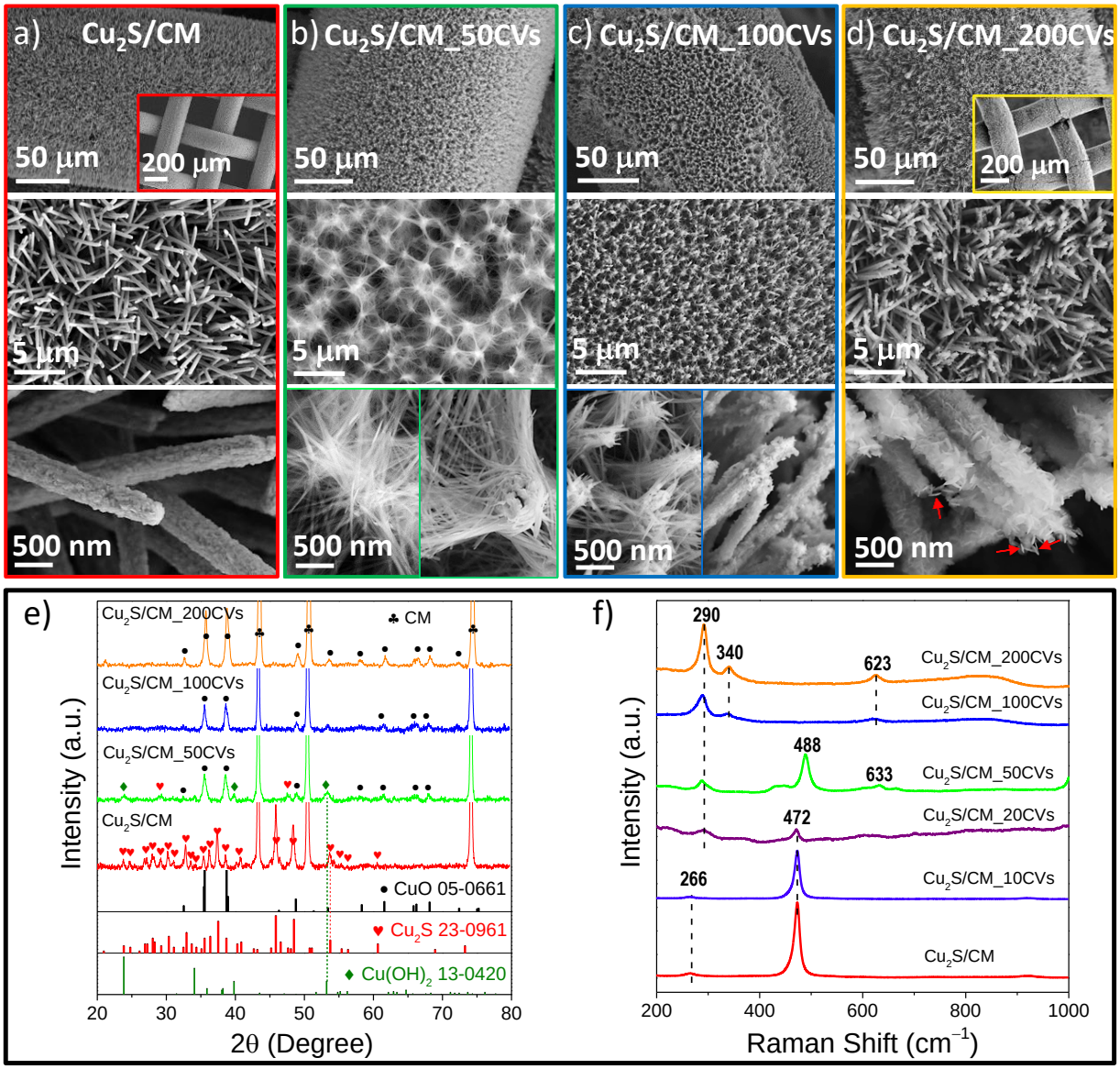


**Figure 3.** (a-d) SEM micrographs of as-prepared $Cu_2S$/CM after different numbers of CVs at a scan rate of 100 mV/s: (a) initial; (b) after 50 CVs; (c) after 100 CVs; (d) after 200 CVs. (e) XRD patterns of as-prepared $Cu_2S$/CM and after a different number of CVs at a scan rate of 100 mV/s. (f) In-situ Raman spectra of as-prepared $Cu_2S$/CM and after 10, 20, 50, 100, and 200 CVs at 100 mV/s.

A fresh $Cu_2S$/CM was cycled for 50 CV at 100 mV/s and afterward operated at a current density of 10 mA/cm$^2$ for 10000 s within a 1M KOH water solution. After these two steps, $Cu_2S$ had fully transformed into CuO (Figure 4a). SEM characterization showed the surface morphology of the final material to consist in nanoflake-based NWs as those obtained after extensive cycling (Figure 4b-d). XPS analysis further confirmed the evolution from $Cu_2S$ to CuO

after the two steps. The measured shift of the Cu 2p doublet to higher binding energies, from 932.7 eV to 933.6 eV (Cu $2p_{3/2}$), was associated to the $Cu^{+}$ to $Cu^{2+}$ oxidation (Figure 4e). According to XPS analysis (Figure 4e, Table S1), the initial $Cu_2S$/CM sample contained 90 % of $Cu_2S$ and 10 % CuO ascribed to surface oxidation as aforementioned. This composition changed to 70 % $Cu(OH)_2$, 18 % CuO and 12 % $Cu_2S$ after 50 CVs and to 100 % CuO after additional operation at 10 mA/$cm^2$ for 10000 s. Besides, the S 2p peak intensity decreased drastically after operation at 10 mA/$cm^2$ for 10000 s, corroborating the chemical transformation of the sulfide to an oxide. Interestingly, small amounts of S remained after long term operation, *ca.* 10 % with respect to Cu, with a relative amount of sulfate significantly increasing, up to a 70 % of the total detected sulfur.[45,62]

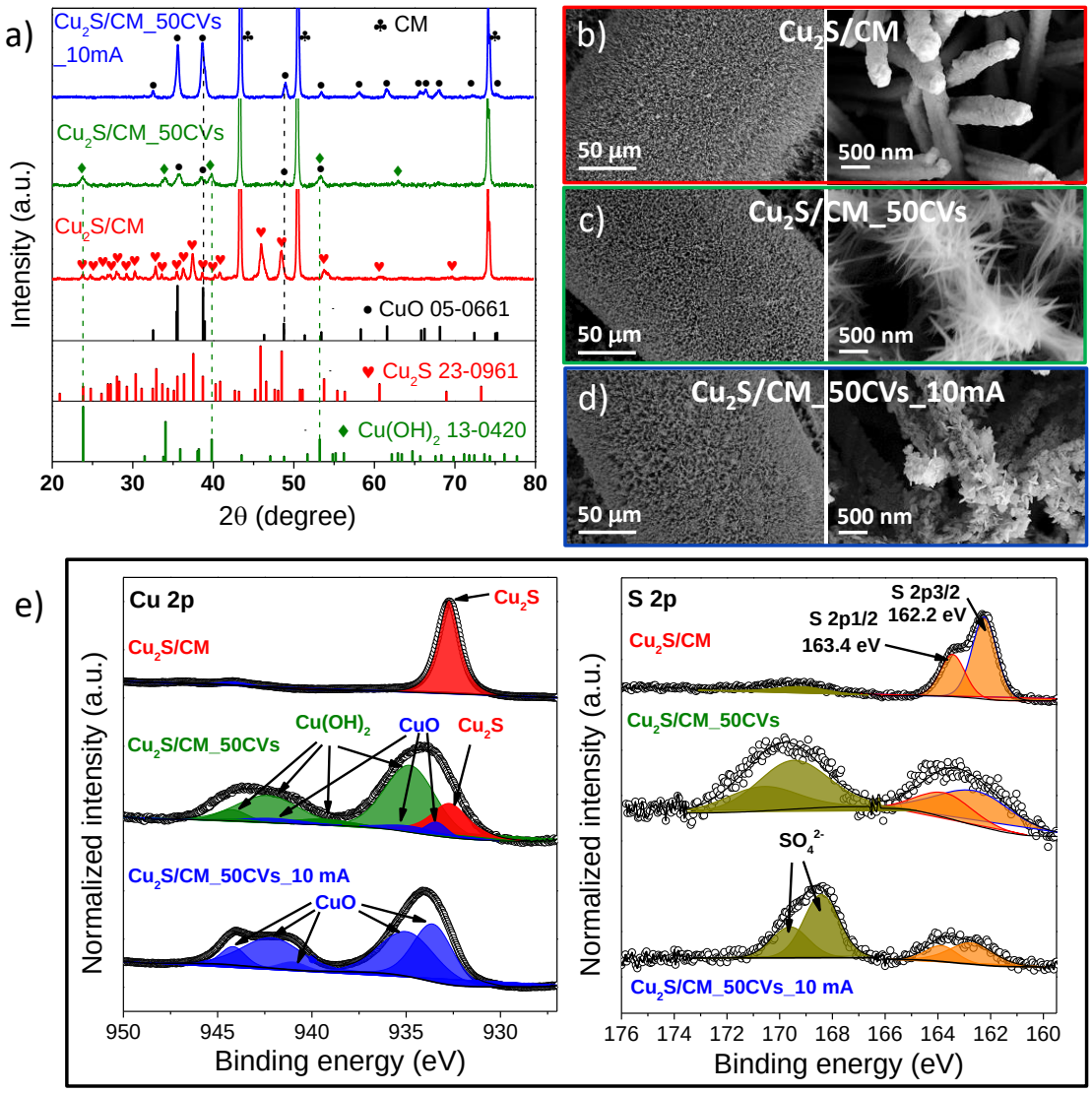


**Figure 4**. (a) XRD patterns and (b-d) SEM images of fresh $Cu_2S$/CM, after 50 CVs ($Cu_2S$/CM_50CVs), and after additional operation at 10 mA for 10000s ($Cu_2S$/CM_50CVs_10mA). (e) Normalized Cu 2p region and S 2p region of the XPS spectra of $Cu_2S$/CM, $Cu_2S$/CM_50CVs and $Cu_2S$/CM_50CVs_10mA samples.

EELS compositional maps showed a homogeneous distribution of Cu and oxygen throughout the grown nanostructures (Figure 5a,c). Additional HRTEM characterization further confirmed the formation of $Cu(OH)_2$ after 50 CVs, with the additional presence of CuO and $Cu_2O$ minor phases (Figure 5b and S4). We associated the appearance of $Cu_2O$ herein to the reduction of CuO under the electron beam, consistently with previous reports.[67] All these phases transformed into

$Cu_xO$ after long-term operation at 10 mA/cm$^2$. HRTEM characterization identified the $Cu_xO$ phase as CuO (Figure 5d), which matched well with results obtained by XRD.

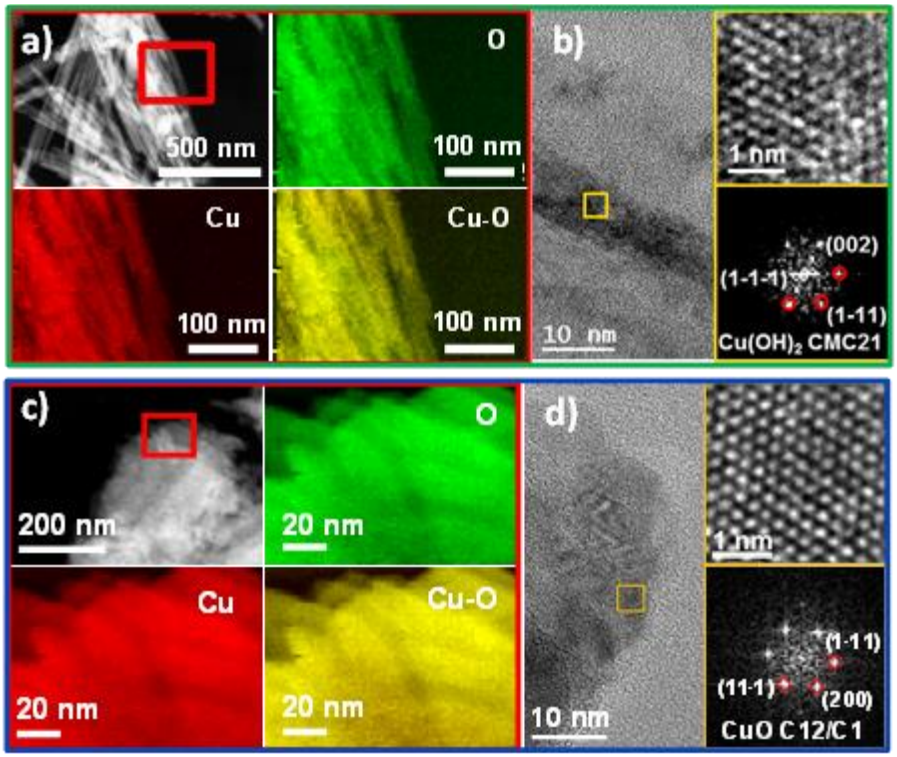


**Figure 5.** (a) EELS chemical composition maps obtained from the red squared area in the STEM micrograph of $Cu_2S$/CM_50CVs. Individual Cu $L_{2,3}$-edges at 931 eV (red) and O K-edges at 532 eV (green) as well as their composites of Cu-O. (b) HRTEM micrograph of a $Cu_2S$/CM_50CVs NW, detail of the orange squared region and its corresponding power spectrum visualized along its [110] zone axis. (c) EELS chemical composition maps obtained from the red squared area in the STEM micrograph of $Cu_2S$/CM_50CVs_10mA. Individual Cu $L_{2,3}$-edges at 931 eV (red) and O K-edge at 532 eV (green) as well as its composite. (d) HRTEM micrograph of a $Cu_2S$/CM_50CVs_10mA NW, detail of the orange squared region and its corresponding power spectrum visualized along its [011] zone axis.

A fresh $Cu_2S$/CM was operated in a 1M KOH solution at 10 mA/cm$^2$ for 10000 s without CV preconditioning (Figure 6). Chronopotentiometry curves (Figure 6a) showed the potential required to maintain 10 mA/cm$^2$ to increase drastically during the initial *ca.* 2000 s, and to stay stable at longer operation times. Initially, no bubbles evolved from the working electrode. However, distinct bubbles started to appear after *ca.* 2000 s. During this time, the initial black CM surface changed to slightly green, which we attributed to the formation of $Cu(OH)_2$, to later become black again. XRD analysis showed the final material to consist in CuO (Figure S5a). SEM analysis showed the final surface to consist on flaked NWs as those obtained after cycling,

but presenting more cracks than when the electrode was pre-cycled (Figure S5b-c). After 10000 s operation, CuO/CM was cycled at 5 mV/s, showing an overpotential of 378 mV ($\eta_{corrected}$ = 336 mV) when delivering a geometric current density of 10 mA/cm$^2$ (Figure 6b).

According to previous reports, the $Cu^{2+}$-$Cu^{3+}$ redox is at the basis of the OER mechanism on CuO/CM electrodes, being $Cu^{3+}$ species the catalytically active sites for oxygen evolution.[68–70] The cathodic peak at *ca.* 1.52 V (0.59 V *vs.* Hg/HgO) obtained on the OER curve of $Cu_2S$-derived CuO/CM (Figure 6b), was attributed to the reduction of $Cu^{3+}$ to $Cu^{2+}$.[68–70] The anodic peak corresponding to the oxidation of $Cu^{2+}$/$Cu^{3+}$ that should appear at *ca.* 0.7 V *vs.* Hg/HgO[70] was not visible in our CVs due to its overlap with the high OER current density. The following mechanism, involving the intermediates OH, OOH, O and $O_2$ adsorbed on an active site M, was proposed for OER in CuO: [68,71]

$$M + OH^- \rightarrow M\text{-}OH + e^-$$

$$M\text{-}OH + OH^- \rightarrow M\text{-}O + H_2O + e^-$$

$$M\text{-}O + OH^- \rightarrow M\text{-}OOH + e^-$$

$$M\text{-}OOH + OH^- \rightarrow M\text{-}OO + H_2O + e^-$$

$$M\text{-}OO \rightarrow M + O_2$$

The generation of M-OH or M-OOH is the crucial step in the formation of $O_2$ and in the extensive oxidation of $Cu_2S$ to $Cu(OH)_2$ and CuO. Being CuO more thermodynamically stable than $Cu(OH)_2$, $K_{sp}$ is $10^{-20.36}$ *vs.* $10^{-19.34}$,[72] CuO/CM is the final composition after relatively long operation of $Cu_2S$/CM under OER conditions.

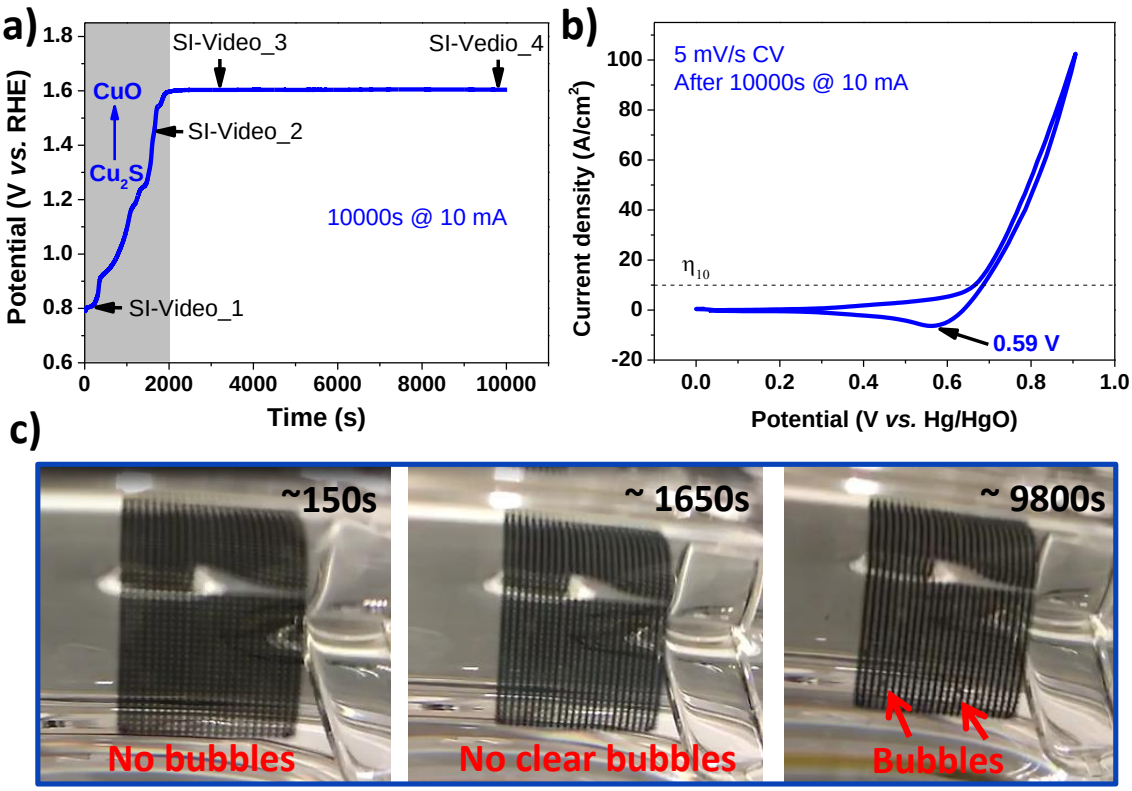


**Figure 6.** (a) Chronopotentiometry curve of $Cu_2S$/CM at a geometric current density of 10 mA/cm$^2$ in 1 M KOH. No CV preconditioning was performed on this sample. (b) Quasi-stationary OER polarization CV at a scan rate of 5 mV/s of $Cu_2S$/CM after 10000 s at 10 mA. (c) Video frames of a $Cu_2S$/CM working electrode showing the evolution or not of bubbles at different times during OER operation.

To compare the OER performance of $Cu_2S$-derived CuO/CM, additional $Cu(OH)_2$/CM were produced by oxidizing CM in a NaOH/APS solution, and additional CuO/CM electrodes were obtained by annealing $Cu(OH)_2$/CM under argon (CuO/CM_AN, see experimental section for details). $Cu(OH)_2$/CM layers directly obtained from the immersion of CM into a NaOH/APS solution contained free standing faceted NWs as described above. The morphology of these $Cu(OH)_2$ was preserved for several dozens of CVs, but cracks appeared after additional CVs (Figure S6). XRD analysis showed $Cu(OH)_2$ NWs to partially transform into CuO after 150 CVs (Figure S7). Notice the conversion of $Cu(OH)_2$ NWs directly grown of the surface of CM was much slower than that of $Cu(OH)_2$ NWs derived from $Cu_2S$ NWs. We associate this experimental result to the much better crystallinity of the former and to the low concentration of grain boundaries in $Cu(OH)_2$ NWs directly grown from CM. Besides, CuO/CM_AN electrodes displayed the presence of smooth NWs (Figure S8a), which appeared attached together after 50

CVs (Figure S8b). After additional cycles, CuO NWs started to break, and after long term chronopotentiometric measurements they detached from CM (Figure S8c-d). It should be noticed that directly formed $Cu(OH)_2$/CM and CuO/CM_AN electrodes did not display the same dramatic evolution of the CVs obtained for $Cu_2S$/CM during the first several cycles (Figures S9-10).

Figure 7a displays quasi-stationary polarization CV curves from CM and from directly obtained $Cu(OH)_2$/CM_100 CVs, CuO/CM-AN_100 CVs, and $Cu_2S$-derived CuO/CM_200 CVs at a scan rate of 5 mV/s. Bare CM showed very poor activity toward OER, requiring an overpotential of 526 mV to deliver a geometric current density of 10 mA/cm$^2$. $Cu_2S$-derived CuO/CM required 380 mV ($\eta_{corrected}$ = 338 mV) to reach 10 mA/cm$^2$, well below the overpotential required by $Cu(OH)_2$/CM_100 CVs ($\eta$=484 mV) and CuO/CM_100 CVs ($\eta$=441 mV). $Cu_2S$-derived CuO/CM electrodes also displayed much lower Tafel slopes, 96 mV/dec, than the other electrodes measured (Figure 7b-c), suggesting a more favorable OER kinetics.

ECSA and EIS measurements were carried out to further understand the improved OER activity of $Cu_2S$-derived CuO/CM electrodes. The relative ECSA was estimated through measurement of the double-layer capacitances ($C_{dl}$) at the solid/liquid interface.[73] Since the current density is only ascribed to the charging of the double layer in the non-Faradaic region, CVs with different scan rates (10 mV/s-150 mV/s) were obtained in the region of 1.22-1.32 V (*vs.* RHE), and the non-Faradaic capacitive current density ($i_c$) was determined by the interval ($\Delta J$) between anodic and cathodic current density calculated from Figure S11. $C_{dl}$ values for $Cu_2S$/CM_100CVs and CuO/CM-AN_100 CVs, calculated using $i_c=\Delta J/2 = \nu \times C_{dl}$, were 93 and 47 mF/cm$^2$, respectively. This result suggested a much higher surface roughness for $Cu_2S$-derived CuO/CMs than directly obtained CuO/CM-AN (Figures S11 and 7d).

Nyquist plots of the impedance response measured at 0.68 V *vs.* Hg/HgO of $Cu_2S$/CM_200CVs and CuO/CM-AN_100CVs are shown in Figure 7e. Qualitatively speaking, $Cu_2S$/CM_200CVs exhibited a smaller semicircle radius compared with that of CuO/CM-AN_100CVs, indicating a smaller charge transfer resistance.[74,75] Impedance responses were fitted with an equivalent circuit containing a series resistance $R_S$, a charge transfer resistance $R_{ct}$, and a constant phase element CPE (Figure 7e, inset).[74,76] Fitting results unambiguously revealed

a clearly enhanced charge transfer process on $Cu_2S$/CM_200CVs, with a $R_{ct}$ of 146 Ω, than on CuO/CM-AN_100CVs, with an order of magnitude higher $R_{ct}$, 1288 Ω.

As shown in Figure 7f, the overpotential required by $Cu_2S$-derived CuO/CM electrodes to deliver a geometric current density of 10 mA/cm$^2$ remained unchanged after 10000 s. Besides, no obvious change on CV behavior occurred after long-term stability test (Figure 2d), indicating remarkable stable electrochemical activity toward OER. On the other hand, the overpotential of $Cu(OH)_2$/CM_100CVs electrode clearly increased from the very beginning of the durability test, manifesting a moderate stability for water electrolysis. As for the CuO/CM-AN_100CVs electrode, it showed a good stability in the initial *ca.* 2000 s, but after this time period, the overpotential strongly increased, which we associated with the detachment of CuO from the CM (Figure S8d).

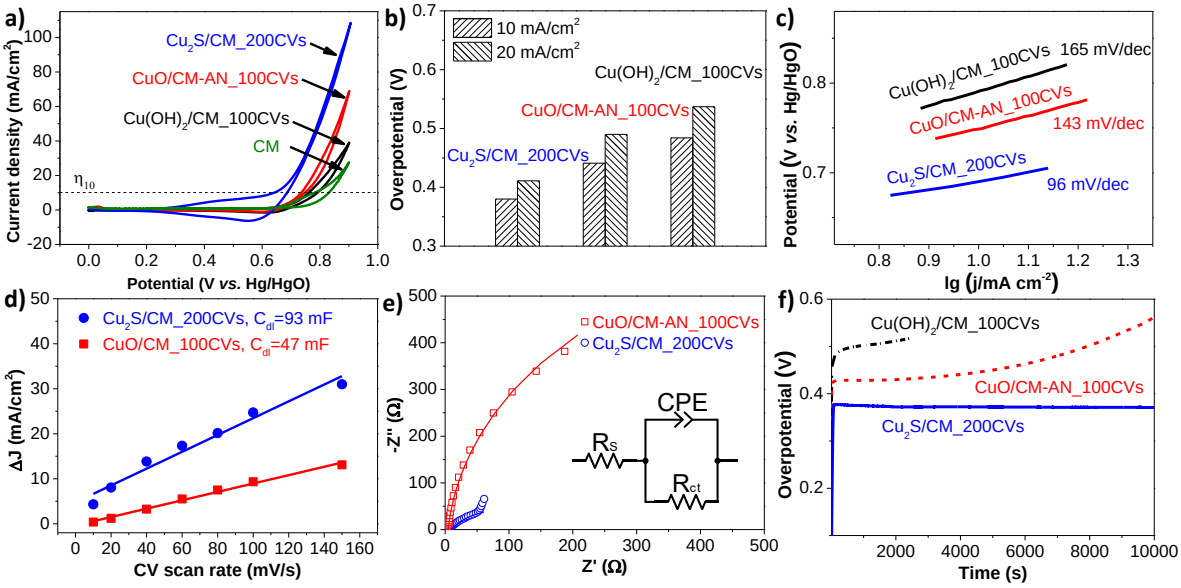


**Figure 7**. Electrocatalytic measurements of OER activity of CV activated $Cu(OH)_2$/CM_100CVs (**Black line**), CuO/CM-AN_100CVs (**Red line**) and $Cu_2S$/CM_200CVs (**Blue line**) in 1.0 M KOH. (a) Quasi-stationary OER polarization CV curves (scan rate: 5 mV/s, without iR corrected). (b) OER catalytic activity diagram. (c) Tafel slope. (d) Capacitive current densities at 1.27 V *vs.* RHE as a function of scan rate of CuO/CM-AN_100CVs and $Cu_2S$/CM_200CVs. (e) Nyquist plots of CuO/CM-AN_100CVs and $Cu_2S$/CM_200CVs with corresponding fitting curves and equivalent circuit. (f) Chronopotentiometric curves at constant current density of 10mA/cm$^2$. $Cu_2S$/CM_200CVs can be also named as CuO/CM-EOT herein based on the discussion. Electrolyte: 1 M KOH.

To improve the catalytic performance of $Cu_2S$-derived CuO/CM, the CM was replaced by a CF, which provided a larger surface area. CV curves measured from $Cu_2S$/CF displayed a similar evolution in the first several cycles, indicating the transition from $Cu_2S$/CF to CuO/CF via $Cu(OH)_2$/CF intermediate (Figure S12). This result was confirmed by XRD and SEM analysis that displayed a similar structural and morphological evolution as that described for $Cu_2S$/CM (Figures 8a,d and S13). OER performance was improved after CV activation, reaching an overpotential down to 328 mV ($\eta_{corrected}$ = 286 mV) to deliver a geometric current density of 10 mA/cm$^2$, and a Tafel slope of 87 mV/dec (Figure 8b). A remarkable durability for 16 h was also measured (Figure 8c and inset). These results place $Cu_2S$-derived CuO/CF among the best Cu-based OER catalysts, with even better performance than numerous nickel/cobalt-based catalysts previously reported (Table S2).

This high performance was associated to several advantages of the $Cu_2S$-derived electrocatalyst, namely: a) Improved adhesion of the active layer to copper when mediating an intermediate sulfurization step; b) Increased surface area associated with the nanostructuration of the NWs; c) Lower charge transfer resistance associated with the higher surface area and the larger density or higher activity of the newly formed catalytic sites; d) the presence of additional catalytic sites. In this last direction, recent reports indicated that in metal sulfides, oxidized S species can remain on the surface for a long period of time and are favorable for OER catalytic activity by tuning the adsorption free energy of the reaction intermediates on the metal sites.[45–48]

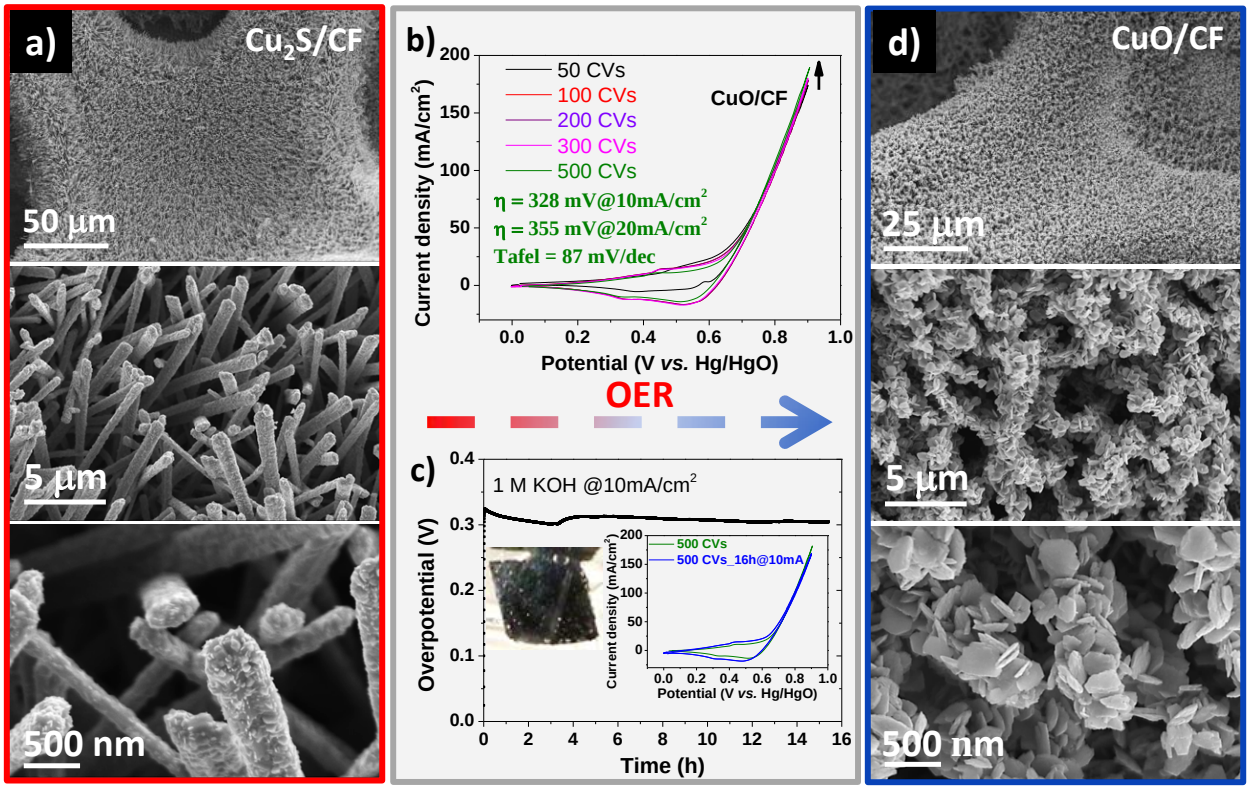


**Figure 8.** (a) SEM images of $Cu_2S$/CF before electrochemical tests. (b) Quasi-stationary OER polarization CV curves (scan rate: 5 mV/s, without iR correction) of $Cu_2S$/CF after different CV activation cycles. (c) Long term chronopotentiometric curve at constant current density of 10mA/cm$^2$ for 16 h; Inset photograph shows oxygen bubbles evolving from the working electrode during OER (see SI-Video_5 for more details). Inset graph shows the quasi-stationary OER polarization CV before and after chronopotentiometry. (d) SEM images of transformed CuO/CF-EOT after chronopotentiometry.

## 4. CONCLUSIONS

In summary, we reported on the chemical, structural and morphological *in situ* transformation of $Cu_2S$/CM into CuO/CM during OER via $Cu(OH)_2$ intermediate. $Cu_2S$-derived CuO/CM displayed enhanced electrochemical OER activity than its precursor $Cu(OH)_2$/CM and directly annealed CuO/CM-AN. $Cu_2S$-derived CuO/CF displayed an overpotential of 286 mV to deliver a geometric current density of 10 mA/cm$^2$, surpassing most Cu-based OER electrocatalysts previously reported. Improved performance with respect to CuO produced from the annealing of $Cu(OH)_2$ NWs was associated to: i) a more stable attachment of the active layer to the current collector; ii) a higher surface area; iii) a lower charge transfer resistance; iv) the presence of

sulphate ions that may act as catalytic active centers. We believe this work provides insights for the fabrication of more effective metal oxide OER catalysts using a simple electrochemical oxidation process. This strategy may be also extended not only to other sulfides and chalcogenides, but even to phosphide and nitride catalysts. Additionally, based on these results, we suggest the necessity to reconsider the chemical composition and associated OER performance of previously reported sulfide OER catalysts in alkaline media.

## ASSOCIATED CONTENT

### Supporting Information

Electronic supplementary information (ESI) available: Additional EDX, SEM, XRD, TEM, electrochemical measurements, table of sample components calculated from XPS and AES, and table of activity comparisons of OER electrocatalysts.

## AUTHOR INFORMATION


### Corresponding Author

*Email: acabot@irec.cat.


### Notes

The authors declare no competing financial interest.

## ACKNOWLEDGMENTS


This work was supported by the European Regional Development Funds and by the Spanish Ministerio de Economí a y Competitividad through the project SEHTOP (ENE2016- 77798-C4-3-R). Y.Z., Junshan Li, R.D., X.H., and T.Z. thank the China Scholarship Council for the scholarship support. Y.L. and N.G. thank the Swiss National Science Foundation (SNF) for funding under the Ambizione Energy grant no. PZENP2_166871. Jordi Llorca is a Serra Hunter Fellow and is´ grateful to ICREA Academia program and to GC 2017 SGR 128. ICN2 acknowledges funding from Generalitat de Catalunya 2017 SGR 327 and the Spanish MINECO project ENE2017-85087-C3. ICN2 is supported by the Severo Ochoa program from the Spanish MINECO (grant no. SEV-2017- 0706) and is funded by the CERCA Programme/Generalitat de Catalunya. Part of the present work has been performed in the framework of Universitat Autònoma de Barcelona Materials Science PhD program.


## REFERENCES


(1) Cabán-Acevedo, M.; Stone, M. L.; Schmidt, J. R.; Thomas, J. G.; Ding, Q.; Chang, H. C.; Tsai, M. L.; He, H.; Jin, S. Efficient Hydrogen Evolution Catalysis Using Ternary Pyrite-

Type Cobalt Phosphosulphide. *Nat. Mater.* **2015**, *14* (12), 1245–1251.

(2) Jin, S. Are Metal Chalcogenides, Nitrides, and Phosphides Oxygen Evolution Catalysts or Bifunctional Catalysts? *ACS Energy Lett.* **2017**, *2* (8), 1937–1938.

(3) Wang, H.-F.; Tang, C.; Zhang, Q. A Review of Precious-Metal-Free Bifunctional Oxygen Electrocatalysts: Rational Design and Applications in Zn−Air Batteries. *Adv. Funct. Mater.* **2018**, *28* (46), 1803329.

(4) Zou, X.; Goswami, A.; Asefa, T. Efficient Noble Metal-Free (Electro)Catalysis of Water and Alcohol Oxidations by Zinc-Cobalt Layered Double Hydroxide. *J. Am. Chem. Soc.* **2013**, *135* (46), 17242–17245.

(5) Li, D.; Baydoun, H.; Verani, C. N.; Brock, S. L. Efficient Water Oxidation Using CoMnP Nanoparticles. *J. Am. Chem. Soc.* **2016**, *138* (12), 4006–4009.

(6) Gao, R.; Li, G. D.; Hu, J.; Wu, Y.; Lian, X.; Wang, D.; Zou, X. In Situ Electrochemical Formation of NiSe/NiOx Core/Shell Nano-Electrocatalysts for Superior Oxygen Evolution Activity. *Catal. Sci. Technol.* **2016**, *6* (23), 8268–8275.

(7) Dutta, A.; Samantara, A. K.; Dutta, S. K.; Jena, B. K.; Pradhan, N. Surface-Oxidized Dicobalt Phosphide Nanoneedles as a Nonprecious, Durable, and Efficient OER Catalyst. *ACS Energy Lett.* **2016**, *1* (1), 169–174.

(8) Zhang, J.; Wang, T.; Pohl, D.; Rellinghaus, B.; Dong, R.; Liu, S.; Zhuang, X.; Feng, X. Interface Engineering of MoS2/Ni3S2Heterostructures for Highly Enhanced Electrochemical Overall-Water-Splitting Activity. *Angew. Chemie - Int. Ed.* **2016**, *55* (23), 6702–6707.

(9) Song, F.; Schenk, K.; Hu, X. A Nanoporous Oxygen Evolution Catalyst Synthesized by Selective Electrochemical Etching of Perovskite Hydroxide CoSn(OH)6 Nanocubes. *Energy Environ. Sci.* **2016**, *9* (2), 473–477.

(10) Jia, X.; Zhao, Y.; Chen, G.; Shang, L.; Shi, R.; Kang, X.; Waterhouse, G. I. N.; Wu, L. Z.; Tung, C. H.; Zhang, T. Ni3FeN Nanoparticles Derived from Ultrathin NiFe-Layered Double Hydroxide Nanosheets: An Efficient Overall Water Splitting Electrocatalyst. *Adv. Energy Mater.* **2016**, *6* (10), 1502585.

(11) Jin, Y.; Wang, H.; Li, J.; Yue, X.; Han, Y.; Shen, P. K.; Cui, Y. Porous MoO 2 Nanosheets as Non-Noble Bifunctional Electrocatalysts for Overall Water Splitting. *Adv. Mater.* **2016**, *28* (19), 3785–3790.

(12) Yan, X.; Li, K.; Lyu, L.; Song, F.; He, J.; Niu, D.; Liu, L.; Hu, X.; Chen, X. From Water Oxidation to Reduction: Transformation from $Ni_x Co_{3-x} O_4$ Nanowires to $NiCo/NiCoO_x$ Heterostructures. *ACS Appl. Mater. Interfaces* **2016**, *8* (5), 3208–3214.

(13) Liu, Y.; Liang, X.; Gu, L.; Zhang, Y.; Li, G. D.; Zou, X.; Chen, J. S. Corrosion Engineering towards Efficient Oxygen Evolution Electrodes with Stable Catalytic Activity for over 6000 Hours. *Nat. Commun.* **2018**, *9* (1), 2609.

(14) McCrory, C. C. L.; Jung, S.; Ferrer, I. M.; Chatman, S. M.; Peters, J. C.; Jaramillo, T. F. Benchmarking Hydrogen Evolving Reaction and Oxygen Evolving Reaction Electrocatalysts for Solar Water Splitting Devices. *J. Am. Chem. Soc.* **2015**, *137* (13), 4347–4357.

(15) Browne, M. P.; Sofer, Z.; Pumera, M. Layered and Two Dimensional Metal Oxides for Electrochemical Energy Conversion. *Energy Environ. Sci.* **2019**, *12* (1), 41–58.

(16) He, P.; Yu, X. Y.; Lou, X. W. D. Carbon-Incorporated Nickel–Cobalt Mixed Metal Phosphide Nanoboxes with Enhanced Electrocatalytic Activity for Oxygen Evolution. *Angew. Chemie - Int. Ed.* **2017**, *56* (14), 3897–3900.

(17) Qiu, B.; Cai, L.; Wang, Y.; Lin, Z.; Zuo, Y.; Wang, M.; Chai, Y. Fabrication of Nickel–Cobalt Bimetal Phosphide Nanocages for Enhanced Oxygen Evolution Catalysis. *Adv. Funct. Mater.* **2018**, *28* (17), 1706008.

(18) Yu, X. Y.; Feng, Y.; Guan, B.; Lou, X. W. D.; Paik, U. Carbon Coated Porous Nickel Phosphides Nanoplates for Highly Efficient Oxygen Evolution Reaction. *Energy Environ. Sci.* **2016**, *9* (4), 1246–1250.

(19) Xu, K.; Chen, P.; Li, X.; Tong, Y.; Ding, H.; Wu, X.; Chu, W.; Peng, Z.; Wu, C.; Xie, Y. Metallic Nickel Nitride Nanosheets Realizing Enhanced Electrochemical Water Oxidation. *J. Am. Chem. Soc.* **2015**, *137* (12), 4119–4125.

(20) Wang, Y.; Liu, D.; Liu, Z.; Xie, C.; Huo, J.; Wang, S. Porous Cobalt-Iron Nitride Nanowires as Excellent Bifunctional Electrocatalysts for Overall Water Splitting. *Chem. Commun.* **2016**, *52* (85), 12614–12617.

(21) Wang, Y.; Zhang, B.; Pan, W.; Ma, H.; Zhang, J. 3 D Porous Nickel–Cobalt Nitrides Supported on Nickel Foam as Efficient Electrocatalysts for Overall Water Splitting. *ChemSusChem* **2017**, *10* (21), 4170–4177.

(22) Wang, Y.; Xie, C.; Liu, D.; Huang, X.; Huo, J.; Wang, S. Nanoparticle-Stacked Porous Nickel-Iron Nitride Nanosheet: A Highly Efficient Bifunctional Electrocatalyst for Overall Water Splitting. *ACS Appl. Mater. Interfaces* **2016**, *8* (29), 18652–18657.

(23) Hou, Y.; Lohe, M. R.; Zhang, J.; Liu, S.; Zhuang, X.; Feng, X. Vertically Oriented Cobalt Selenide/NiFe Layered-Double-Hydroxide Nanosheets Supported on Exfoliated Graphene Foil: An Efficient 3D Electrode for Overall Water Splitting. *Energy Environ. Sci.* **2016**, *9* (2), 478–483.

(24) Xu, R.; Wu, R.; Shi, Y.; Zhang, J.; Zhang, B. Ni3Se2 Nanoforest/Ni Foam as a Hydrophilic, Metallic, and Self-Supported Bifunctional Electrocatalyst for Both H2 and O2 Generations. *Nano Energy* **2016**, *24*, 103–110.

(25) Xiong, D.; Zhang, Q.; Thalluri, S. M.; Xu, J.; Li, W.; Fu, X.; Liu, L. One-Step Fabrication of Monolithic Electrodes Comprising Co9S8 Particles Supported on Cobalt Foam for Efficient and Durable Oxygen Evolution Reaction. *Chem. - A Eur. J.* **2017**, *23* (36), 8749–8755.

(26) Dong, B.; Zhao, X.; Han, G. Q.; Li, X.; Shang, X.; Liu, Y. R.; Hu, W. H.; Chai, Y. M.; Zhao, H.; Liu, C. G. Two-Step Synthesis of Binary Ni-Fe Sulfides Supported on Nickel Foam as Highly Efficient Electrocatalysts for the Oxygen Evolution Reaction. *J. Mater. Chem. A* **2016**, *4* (35), 13499–13508.

(27) Zhu, W.; Yue, X.; Zhang, W.; Yu, S.; Zhang, Y.; Wang, J.; Wang, J. Nickel Sulfide Microsphere Film on Ni Foam as an Efficient Bifunctional Electrocatalyst for Overall Water Splitting. *Chem. Commun.* **2016**, *52* (7), 1486–1489.

(28) Ma, X.; Zhang, W.; Deng, Y.; Zhong, C.; Hu, W.; Han, X. Phase and Composition Controlled Synthesis of Cobalt Sulfide Hollow Nanospheres for Electrocatalytic Water Splitting. *Nanoscale* **2018**, *10* (10), 4816–4824.

(29) Huynh, M.; Bediako, D. K.; Nocera, D. G. A Functionally Stable Manganese Oxide Oxygen Evolution Catalyst in Acid. *J. Am. Chem. Soc.* **2014**, *136* (16), 6002–6010.

(30) Ryu, J.; Jung, N.; Jang, J. H.; Kim, H. J.; Yoo, S. J. In Situ Transformation of Hydrogen-Evolving CoP Nanoparticles: Toward Efficient Oxygen Evolution Catalysts Bearing Dispersed Morphologies with Co-Oxo/Hydroxo Molecular Units. *ACS Catal.* **2015**, *5* (7), 4066–4074.

(31) Reddy, N. K.; Winkler, S.; Koch, N.; Pinna, N. Electrochemical Water Oxidation of Ultrathin Cobalt Oxide-Based Catalyst Supported onto Aligned ZnO Nanorods. *ACS Appl. Mater. Interfaces* **2016**, *8* (5), 3226–3232.

(32) Zhu, Y.; Chen, H. C.; Hsu, C. S.; Lin, T. S.; Chang, C. J.; Chang, S. C.; Tsai, L. D.; Chen, H. M. Operando Unraveling of the Structural and Chemical Stability of P-Substituted CoSe 2 Electrocatalysts toward Hydrogen and Oxygen Evolution Reactions in Alkaline Electrolyte. *ACS Energy Lett.* **2019**, *4* (4), 987–994.

(33) Feng, X.; Jiao, Q.; Liu, T.; Li, Q.; Yin, M.; Zhao, Y.; Li, H.; Feng, C.; Zhou, W. Facile Synthesis of Co 9 S 8 Hollow Spheres as a High-Performance Electrocatalyst for the Oxygen Evolution Reaction. *ACS Sustain. Chem. Eng.* **2018**, *6* (2), 1863–1871.

(34) Wygant, B. R.; Kawashima, K.; Mullins, C. B. Catalyst or Precatalyst? The Effect of Oxidation on Transition Metal Carbide, Pnictide, and Chalcogenide Oxygen Evolution Catalysts. *ACS Energy Lett.* **2018**, *3* (12), 2956–2966.

(35) Mabayoje, O.; Shoola, A.; Wygant, B. R.; Mullins, C. B. The Role of Anions in Metal Chalcogenide Oxygen Evolution Catalysis: Electrodeposited Thin Films of Nickel Sulfide as "Pre-Catalysts." *ACS Energy Lett.* **2016**, *1* (1), 195–201.

(36) Lian, Y.; Sun, H.; Wang, X.; Qi, P.; Mu, Q.; Chen, Y.; Ye, J.; Zhao, X.; Deng, Z.; Peng, Y. Carved Nanoframes of Cobalt-Iron Bimetal Phosphide as a Bifunctional Electrocatalyst for Efficient Overall Water Splitting. *Chem. Sci.* **2019**, *10* (2), 464–474.

(37) Xu, J.; Li, J.; Xiong, D.; Zhang, B.; Liu, Y.; Wu, K. H.; Amorim, I.; Li, W.; Liu, L. Trends in Activity for the Oxygen Evolution Reaction on Transition Metal (M = Fe, Co, Ni) Phosphide Pre-Catalysts. *Chem. Sci.* **2018**, *9* (14), 3470–3476.

(38) Zhang, Y.; Ouyang, B.; Xu, J.; Jia, G.; Chen, S.; Rawat, R. S.; Fan, H. J. Rapid Synthesis of Cobalt Nitride Nanowires: Highly Efficient and Low-Cost Catalysts for Oxygen Evolution. *Angew. Chemie - Int. Ed.* **2016**, *55* (30), 8670–8674.

(39) Li, W.; Gao, X.; Xiong, D.; Xia, F.; Liu, J.; Song, W. G.; Xu, J.; Thalluri, S. M.; Cerqueira, M. F.; Fu, X.; et al. Vapor-Solid Synthesis of Monolithic Single-Crystalline CoP Nanowire Electrodes for Efficient and Robust Water Electrolysis. *Chem. Sci.* **2017**, *8* (4), 2952–2958.

(40) Liu, Y.; Li, Q.; Si, R.; Li, G.-D.; Li, W.; Liu, D.-P.; Wang, D.; Sun, L.; Zhang, Y.; Zou, X. Coupling Sub-Nanometric Copper Clusters with Quasi-Amorphous Cobalt Sulfide Yields Efficient and Robust Electrocatalysts for Water Splitting Reaction. *Adv. Mater.* **2017**, *29* (13), 1606200.

(41) Xu, J.; Liu, Y.; Li, J.; Amorim, I.; Zhang, B.; Xiong, D.; Zhang, N.; Thalluri, S. M.; Sousa, J. P. S.; Liu, L. Hollow Cobalt Phosphide Octahedral Pre-Catalysts with Exceptionally High Intrinsic Catalytic Activity for Electro-Oxidation of Water and Methanol. *J. Mater. Chem. A* **2018**, *6* (42), 20646–20652.

(42) Zhang, Y.; Ouyang, B.; Xu, J.; Jia, G.; Chen, S.; Rawat, R. S.; Fan, H. J. Rapid Synthesis of Cobalt Nitride Nanowires: Highly Efficient and Low-Cost Catalysts for Oxygen Evolution. *Angew. Chemie - Int. Ed.* **2016**, *55* (30), 8670–8674.

(43) Xu, X.; Song, F.; Hu, X. A Nickel Iron Diselenide-Derived Efficient Oxygen-Evolution Catalyst. *Nat. Commun.* **2016**, *7* (1), 12324.

(44) Lian, Y.; Sun, H.; Wang, X.; Qi, P.; Mu, Q.; Chen, Y.; Ye, J.; Zhao, X.; Deng, Z.; Peng, Y. Carved Nanoframes of Cobalt-Iron Bimetal Phosphide as a Bifunctional Electrocatalyst for Efficient Overall Water Splitting. *Chem. Sci.* **2019**, *10* (2), 464–474.

(45) Souleymen, R.; Wang, Z.; Qiao, C.; Naveed, M.; Cao, C. Microwave-Assisted Synthesis of Graphene-like Cobalt Sulfide Freestanding Sheets as an Efficient Bifunctional Electrocatalyst for Overall Water Splitting. *J. Mater. Chem. A* **2018**, *6* (17), 7592–7607.

(46) Wu, Z.; Huang, L.; Liu, H.; Wang, H. Element-Specific Restructuring of Anion- and Cation-Substituted Cobalt Phosphide Nanoparticles under Electrochemical Water-Splitting Conditions. *ACS Catal.* **2019**, *9* (4), 2956–2961.

(47) Wang, T.; Nam, G.; Jin, Y.; Wang, X.; Ren, P.; Kim, M. G.; Liang, J.; Wen, X.; Jang, H.; Han, J.; et al. NiFe (Oxy) Hydroxides Derived from NiFe Disulfides as an Efficient Oxygen Evolution Catalyst for Rechargeable Zn–Air Batteries: The Effect of Surface S Residues. *Adv. Mater.* **2018**, *30* (27), 1800757.

(48) Legrand, D. L.; Nesbitt, H. W.; Bancroft, G. M. X-Ray Photoelectron Spectroscopic Study of a Pristine Millerite (NiS) Surface and the Effect of Air and Water Oxidation. *Am. Mineral.* **1998**, *83* (11-12 PART 1), 1256–1265.

(49) Hou, C. C.; Wang, C. J.; Chen, Q. Q.; Lv, X. J.; Fu, W. F.; Chen, Y. Rapid Synthesis of Ultralong Fe(OH)3:Cu(OH)2 Core-Shell Nanowires Self-Supported on Copper Foam as a Highly Efficient 3D Electrode for Water Oxidation. *Chem. Commun.* **2016**, *52* (100),

14470–14473.

(50) Kang, J.; Sheng, J.; Xie, J.; Ye, H.; Chen, J.; Fu, X. Z.; Du, G.; Sun, R.; Wong, C. P. Tubular Cu(OH)2 Arrays Decorated with Nanothorny Co-Ni Bimetallic Carbonate Hydroxide Supported on Cu Foam: A 3D Hierarchical Core-Shell Efficient Electrocatalyst for the Oxygen Evolution Reaction. *J. Mater. Chem. A* **2018**, *6* (21), 10064–10073.

(51) Zhu, S.; Wang, Z.; Huang, F.; Zhang, H.; Li, S. Hierarchical Cu(OH)2@Ni2(OH)2CO3 Core/Shell Nanowire Arrays: In Situ Grown on Three-Dimensional Copper Foam for High-Performance Solid-State Supercapacitors. *J. Mater. Chem. A* **2017**, *5* (20), 9960–9969.

(52) Wang, P.; Qiao, M.; Shao, Q.; Pi, Y.; Zhu, X.; Li, Y.; Huang, X. Phase and Structure Engineering of Copper Tin Heterostructures for Efficient Electrochemical Carbon Dioxide Reduction. *Nat. Commun.* **2018**, *9* (1), 4933.

(53) An, L.; Zhou, P.; Yin, J.; Liu, H.; Chen, F.; Liu, H.; Du, Y.; Xi, P. Phase Transformation Fabrication of a Cu<inf>2</Inf>S Nanoplate as an Efficient Catalyst for Water Oxidation with Glycine. *Inorg. Chem.* **2015**, *54* (7), 3281–3289.

(54) He, L.; Zhou, D.; Lin, Y.; Ge, R.; Hou, X.; Sun, X.; Zheng, C. Ultrarapid in Situ Synthesis of Cu2S Nanosheet Arrays on Copper Foam with Room-Temperature-Active Iodine Plasma for Efficient and Cost-Effective Oxygen Evolution. *ACS Catal.* **2018**, *8* (5), 3859–3864.

(55) Biesinger, M. C. Advanced Analysis of Copper X-Ray Photoelectron Spectra. *Surf. Interface Anal.* **2017**, *49* (13), 1325–1334.

(56) Larson, P. E. X-Ray Induced Photoelectron and Auger Spectra of Cu, CuO, Cu2O, and Cu2S Thin Films. *J. Electron Spectros. Relat. Phenomena* **1974**, *4* (3), 213–218.

(57) Kuo, C. H.; Chu, Y. T.; Song, Y. F.; Huang, M. H. Cu2O Nanocrystal-Templated Growth of Cu2S Nanocages with Encapsulated Au Nanoparticles and in-Situ Transmission X-Ray Microscopy Study. *Adv. Funct. Mater.* **2011**, *21* (4), 792–797.

(58) Fan, M.; Gao, R.; Zou, Y. C.; Wang, D.; Bai, N.; Li, G. D.; Zou, X. An Efficient Nanostructured Copper(I) Sulfide-Based Hydrogen Evolution Electrocatalyst at Neutral PH. *Electrochim. Acta* **2016**, *215*, 366–373.

(59) Folmer, J. C. W.; Jellinek, F. The Valence of Copper in Sulphides and Selenides: An X-Ray Photoelectron Spectroscopy Study. *J. Less-Common Met.* **1980**, *76* (1–2), 153–162.

(60) Nayak, A.; Tsuruoka, T.; Terabe, K.; Hasegawa, T.; Aono, M. Switching Kinetics of a Cu2S-Based Gap-Type Atomic Switch. *Nanotechnology* **2011**, *22* (23), 235201.

(61) Laajalehto, K.; Kartio, I.; Nowak, P. XPS Study of Clean Metal Sulfide Surfaces. *Appl. Surf. Sci.* **1994**, *81* (1), 11–15.

(62) Yang, Y.; Luan, X.; Dai, X.; Zhang, X.; Qiao, H.; Zhao, H.; Yong, J.; Yu, L.; Han, J.; Zhang, J. Partially Sulfurated Ultrathin Nickel-Iron Carbonate Hydroxides Nanosheet

Boosting the Oxygen Evolution Reaction. *Electrochim. Acta* **2019**, *309*, 57–64.

(63) Minceva-Sukarova, B.; Najdoski, M.; Grozdanov, I.; Chunnilall, C. J. Raman Spectra of Thin Solid Films of Some Metal Sulfides. *J. Mol. Struct.* **1997**, *410–411*, 267–270.

(64) Milekhin, A. G.; Yeryukov, N. A.; Sveshnikova, L. L.; Duda, T. A.; Rodyakina, E. E.; Gridchin, V. A.; Sheremet, E. S.; Zahn, D. R. T. Combination of Surface- and Interference-Enhanced Raman Scattering by CuS Nanocrystals on Nanopatterned Au Structures. *Beilstein J. Nanotechnol.* **2015**, *6* (1), 749–754.

(65) Hamilton, J. C. In Situ Raman Spectroscopy of Anodic Films Formed on Copper and Silver in Sodium Hydroxide Solution. *J. Electrochem. Soc.* **2006**, *133* (4), 739.

(66) Chou, M. H.; Liu, S. B.; Huang, C. Y.; Wu, S. Y.; Cheng, C. L. Confocal Raman Spectroscopic Mapping Studies on a Single CuO Nanowire. *Appl. Surf. Sci.* **2008**, *254* (23), 7539–7543.

(67) Long, N. J.; Petford-Long, A. K. In-Situ Electron-Beam-Induced Reduction of CuO: A Study of Phase Transformations in Cupric Oxide. *Ultramicroscopy* **1986**, *20* (1–2), 151–159.

(68) Deng, Y.; Handoko, A. D.; Du, Y.; Xi, S.; Yeo, B. S. In Situ Raman Spectroscopy of Copper and Copper Oxide Surfaces during Electrochemical Oxygen Evolution Reaction: Identification of CuIII Oxides as Catalytically Active Species. *ACS Catal.* **2016**, *6* (4), 2473–2481.

(69) Miller, B. Split-Ring Disk Study of the Anodic Processes at a Copper Electrode in Alkaline Solution. *J. Electrochem. Soc.* **1969**, *116* (12), 1675.

(70) Reyter, D.; Odziemkowski, M.; Bélanger, D.; Roué, L. Electrochemically Activated Copper Electrodes. *J. Electrochem. Soc.* **2007**, *154* (8), K36.

(71) Fan, K.; Zou, H.; Lu, Y.; Chen, H.; Li, F.; Liu, J.; Sun, L.; Tong, L.; Toney, M. F.; Sui, M.; et al. Direct Observation of Structural Evolution of Metal Chalcogenide in Electrocatalytic Water Oxidation. *ACS Nano* **2018**, *12* (12), 12369–12379.

(72) Pichtel, J. Solubility Product Constants at 25°C http://www.aqion.de/site/16 (accessed Apr 11, 2019).

(73) Lu, X.; Zhao, C. Electrodeposition of Hierarchically Structured Three-Dimensional Nickel-Iron Electrodes for Efficient Oxygen Evolution at High Current Densities. *Nat. Commun.* **2015**, *6* (1), 6616.

(74) Zuo, Y.; Liu, Y.; Li, J.; Du, R.; Yu, X.; Xing, C.; Zhang, T.; Yao, L.; Arbiol, J.; Llorca, J.; et al. Solution-Processed Ultrathin SnS 2 -Pt Nanoplates for Photoelectrochemical Water Oxidation. *ACS Appl. Mater. Interfaces* **2019**, *11* (7), 6918–6926.

(75) Zhu, X.; Guijarro, N.; Liu, Y.; Schouwink, P.; Wells, R. A.; Le Formal, F.; Sun, S.; Gao, C.; Sivula, K. Spinel Structural Disorder Influences Solar-Water-Splitting Performance of ZnFe 2 O 4 Nanorod Photoanodes. *Adv. Mater.* **2018**, *30* (34), 1801612.

(76) Liu, Y.; Le Formal, F.; Boudoire, F.; Yao, L.; Sivula, K.; Guijarro, N. Insights into the Interfacial Carrier Behaviour of Copper Ferrite (CuFe 2 O 4 ) Photoanodes for Solar Water Oxidation. *J. Mater. Chem. A* **2019**, *7* (4), 1669–1677.